Improving the Spatial Distribution of Snow Cover Simulations by Assimilation of Satellite Stereoscopic Imagery

César Deschamps-Berger, B. Cluzet, M. Dumont, M. Lafaysse, E. Berthier, P. Fanise, S. Gascoin

Improving the spatial distribution of snow cover simulations by assimilation of satellite stereoscopic imagery

Deschamps-Berger C.[1,2], Cluzet B.[1], Dumont M.[1], Lafaysse M.[1], Berthier E.[3], Fanise P.[2], Gascoin S.[2]

[1] Université Grenoble Alpes, Université de Toulouse, Météo-France, Grenoble, France, CNRS, CNRM, Centre d'Etudes de la Neige, 38000 Grenoble, France.

[2] Centre d'Etudes Spatiales de la Biosphère, CESBIO, Univ. Toulouse, CNES/CNRS/INRA/IRD/UPS, 31401 Toulouse, France.

[3] Centre National de la Recherche Scientifique (CNRS-LEGOS), 31400 Toulouse, France.

Corresponding author: César Deschamps-Berger (cesar.deschamps-berger@protonmail.com)

Key Points:

- Assimilation of one satellite snow depth map corrects bias in precipitation and improves the modeled spatial variability of the snow depth
- In the case of a large bias in precipitation, assimilation of a single snow depth map can modify incidentally the way the SWE and snowpack bulk density are modeled
- This approach, which combines satellite data for assimilation and validation, could be transferred to unmonitored basins

Abstract

Moutain snow cover is highly variable both spatially and temporally and has a tremendous impact on ecosystems and human activities. Numerical models provide continuous estimates of the variability of snow cover properties in time and space. However, they suffer from large uncertainties, for instance originating from errors in the meteorological inputs. Here, we show that the snow depth variability at 250 m spatial resolution can be well simulated by assimilating snow depth maps from satellite photogrammetry in a detailed snowpack model. The assimilation of a single snow depth map per snow season using a particle filter is sufficient to improve the simulated snow depth and its spatial variability, originally poorly represented due to missing physical processes and errors in the precipitation inputs. Assimilation of snow depth only is nevertheless not sufficient for both compensating for strong bias in precipitation and for selecting the most appropriate representation of the physical processes in the snow model. Combined assimilation of snow depths maps and other snow observations is thus a promising avenue for accurate simulations of mountain snow cover.

Plain language summary

Snow in mountains is critical as it controls water availability for ecosystems and human societies, when it is most needed. In the mountains the snow depth is both hard to map due to its spatial variability and crucial to estimate water resources. Nowadays, the best estimations of the snow depth distribution combine models and spatially distributed snow depth measurements. In this work, we build upon this approach by combining a recently developed snow depth mapping method with a state-of-the-art model through assimilation. The assimilation of snow depth maps derived from satellite photogrammetry corrects bias in the precipitation and improves the spatial variability of the simulated snow depth. The workflow presented can be transferred to any mountain range, showing a promising way to study water resources in remote areas.

1 Introduction

The seasonal snowpack in mountain regions controls the seasonality of streamflow, vegetation growth, soil and river temperature (Bard et al., 2015; Choler, 2018; Dedieu et al., 2016; Luce et al., 2014). Accurate knowledge of the spatial distribution of the snowpack properties is necessary to describe the timing and extent of these effects (Freudiger et al., 2017; Hedrick et al., 2018;

Margulis et al., 2019; Revuelto et al., 2016). However, a major challenge is the lack of a direct method to estimate the spatial distribution of snow water equivalent (SWE) in mountain regions (Dozier et al., 2016). Modeling is often used but is limited by the availability of accurate gridded meteorological forcing (Raleigh et al., 2015). The spatial interpolation of meteorological variables (e.g., air temperature, precipitation quantity and phase, and wind) is hampered by the absence of meteorological stations at high elevations (Rasmussen et al., 2012) and by the high spatial variability of meteorological processes in mountain environments due to the complex topography (Barry, 2008). Snowpack models are also prone to errors due to uncertainties in parameter values, the form of parameterizations and the lack of some physical processes (Ménard et al., 2021). Assimilation of gridded data in a snowpack model is key to overcoming these challenges (Girotto et al., 2020; Largeron et al., 2020). It enables taking advantage of the profusion of remotely sensed data, especially satellite data, and improving model outputs by a balanced combination of model states and observations as a function of their estimated uncertainties. Maps of the snow cover area (SCA) are widely available and therefore have been predominantly assimilated to improve the simulation of SWE and snowmelt runoff (e.g., Andreadis & Lettenmaier, 2006; Rodell & Houser, 2004; Thirel et al., 2011; Margulis et al., 2015; Baba et al., 2018). Other gridded products were assimilated, such as SWE maps derived from passive microwave images (Andreadis & Lettenmaier, 2006) or surface reflectance maps (Dumont et al., 2012). But the SCA is only indirectly related to SWE and the low spatial resolution of passive microwave images is limiting, fostering the need for assimilation of other types of data.

HS is a key snowpack variable for hydrological applications, as it can be combined with bulk density to obtain the SWE. Recently, the development of new methods to retrieve snow depth (height of snow, HS) based on lidar or photogrammetric measurements from airborne, drone or satellite platforms has presented new opportunities to better constrain snowpack models. Vögeli et al. (2016) and Brauchli et al. (2017) used an HS map to distribute solid precipitation in a Swiss Alps catchment. They corrected an initial field of precipitation with a multiplicative factor per point based on the ratio of the HS at the point and the average HS of the area. The HS was extracted from a single map measured close to the date of peak SWE by airborne photogrammetry. This computationally simple method increased the spatial variability of the simulated HS and improved the simulated discharge of the basin. Another simple method to

benefit from HS maps is the direct insertion of the HS map in the model. Revuelto et al. (2016) showed that direct insertion of HS maps derived from terrestrial laser scans improved the spatial distribution of modeled HS and the timing of snow melt in a Spanish Pyrenees catchment. However, the area covered with terrestrial laser scans is at best a few square kilometers and was less than 1 km² in that study (Deems et al., 2013). Shaw et al., (2020) used an HS map derived from satellite stereo-imagery to initialize a hydrological model of a 102 km² high-Andean catchment. This improved the simulation of the runoff compared with initialization with a modeled HS map. Lidar measurements of the Airborne Snow Observatory (ASO, Painter et al., 2015) campaigns enabled experiments of direct insertion of HS maps on a larger scale in a mountainous environment (>1000 km²) (Hedrick et al., 2018). Insertion of a dozen HS maps from approximately 1st April and throughout the melt season improved the spatial distribution of modeled HS in several catchments in the western USA (Hedrick et al., 2018). However, the direct insertion of any observed variable can lead to an unrealistic state of the snowpack variables that are not observed (e.g., density and temperature), resulting in a rapid loss of its added value (Viallon-galinier et al., 2020). In addition, grid cells where the model predicts no snow, although the observation indicates that snow is present, require the estimation of the vertical profile of all snow physical properties (e.g. density, temperature). More generally, direct insertion assumes that observations are perfect, which is unrealistic. To avoid this assumption, other methods consider and balance the uncertainties of the observation and of the model. For instance, the particle batch smoother method is applied to ensemble simulations by weighting the ensemble members (the particles) based on their distance to the observation. With the same data as Hedrick et al. (2018), this approach improved the HS spatial distribution up to 75 days after assimilation of a single HS map (Margulis et al., 2019). The particle filter method is similar to the particle batch smoother but can easily be combined with a forecast system. It is well adapted to nonlinear detailed snow models with variable numbers of layers (Cluzet et al., 2021). A particle filter assimilation scheme has been used for point simulations of snowpack either with synthetic (Charrois et al., 2016; Cluzet et al., 2021) or real data (Magnusson et al., 2017; Smyth et al., 2019; Smyth et al., 2020) but, to our knowledge, has never been used with gridded data.

These studies are promising and show how HS maps can improve the simulation of the spatial distribution of snowpack properties. Except for Shaw et al. (2020), these studies relied on highly accurate airborne and terrestrial measurements with standard errors smaller than 0.2 m. This

level of accuracy can only be reached by ground, drone or airborne measurements, which require direct access to, or close to, the field. However, the assimilation of data artificially degraded to lower accuracy still improved point simulation of the snowpack (Smyth et al., 2020). Very high-resolution stereoscopic satellites such as Pléiades or Worldview provide HS maps with a lower accuracy (~0.7 m) than ground, drone or airborne methods but with less logistical constraints and less cost for the end user (Marti et al., 2016; Shaw et al., 2020; Deschamps-Berger et al., 2020; Eberhard et al., 2021). With this method, HS maps are calculated by differencing two digital elevation models derived from stereoscopic images with and without snow. The typical footprint of a single image (20 km x 20 km for Pléiades) is larger than ground and drone products but smaller than airborne products. Pairs or triplets of stereoscopic images are acquired on-demand contrary to optical satellites with a fixed revisit time (e.g. MODIS, Landsat, Sentinel). Multiannual time series of HS maps from satellite photogrammetry have never been used to date for assimilation in a snowpack model.

In this work, we investigate if satellite photogrammetric HS maps can be used to improve snow cover simulations. To this aim, we ran ensemble simulations of the SAFRAN-Crocus snowpack modeling chain (Vernay et al., 2021) in a pilot catchment in the Pyrenees Mountains (France) for five hydrological years at a 250 m spatial resolution. Several processes directly influence the HS such as the amount of precipitation, the density of the fresh snow and the compaction of the snowpack. The uncertainties of these processes are accounted for by using an ensemble of meteorological forcings (e.g. uncertainty of the precipitation) and a multiphysical model (e.g. density of the fresh snow, compaction). A multiphysical model is an ensemble modelling framework in which ensemble members are calculated with different physical parameterizations of most uncertain processes represented in the model (Essery et al., 2013; Lafaysse et al., 2017). We calculated a multiannual time series of six HS maps from stereoscopic images from the Pléiades satellites and assimilated one HS map per year with a particle filter scheme (Cluzet et al., 2021).

Therefore, we tackle two main questions:

1. Is the accuracy of satellite photogrammetric HS maps sufficient to improve the spatial distribution of the HS in a detailed model?

156 2. In case of improvement, does assimilation of the HS correct errors in the meteorological
157 forcings, in the physical parameterizations of the model, or both?

158 The impact of assimilation was evaluated with various independent data: a Pléiades HS map not
159 assimilated, Sentinel-2 and Landsat 8 snow melt-out date (SMOD), MODIS SCA and in situ HS
160 from an automatic meteorological station (Question 1). The impact of the assimilation is also
161 evaluated by comparing the meteorological forcings and the physical parameterization associated
162 with the ensemble members selected by the filter (Question 2).
163

164 **2 Study area**

165 The study site is a 100 km² mountainous area in the Upper Vicdessos Valley in the Pyrenees
166 (Figures 1 and 2), where elevation ranges between 1000 m a.s.l. and 2700 m a.s.l. (Szczypta et
167 al., 2015; Marti et al., 2016). The vegetation is subalpine pine and beech forest and alpine
168 grassland above the tree line at approximately 1800 m a.s.l. (Figure 3 of Vacquie et al., 2016).
169 Small portions of the area contain human infrastructures with a small city (Auzat, <0.5 km²) and
170 a few roads. Ponds and two man-made reservoirs for hydropower production cover
171 approximately 0.3 km². Seasonal snowpack typically sets in November-December and melts
172 between April and June. The study period encompasses five water years (1 September to 31
173 August, WY) from WY 2014-2015 to WY 2018-2019. This period provides various snow
174 conditions as shown by the winter precipitation of the nearby automatic weather statin (AWS)
175 between 2000 and 2019. WY 2018-2019 and WY 2016-2017 had among the lowest winter
176 precipitation (rank number 19 and 17 respectively) while WY 2017-2018 had high winter
177 precipitation (rank number 3). WY 2014-2015 and WY 2015-2016 were close to the median
178 winter precipitation with rank 7 and 11.
179

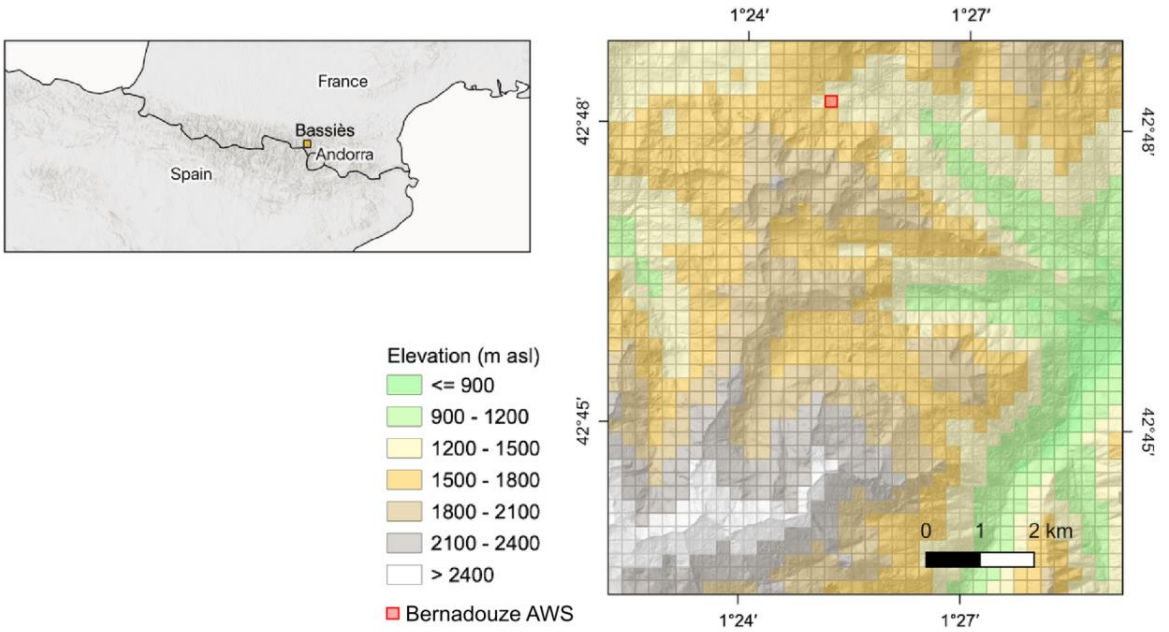

Figure 1. The simulation area in the Upper Vicdessos valley, Pyrenees. The coloured map shows the surface elevation at the resolution of the simulation grid (250 m). The background image is a hillshade view of the topography at high-resolution (3 m).

Figure 2. Photographs taken from Col de la Serrette near the geographic center of the study area (left: 26 October 2014, right: 11 March 2015).

3 Data and methods

3.1. Model and assimilation scheme

The Crocus model simulates snowpack as a stack of 3 to 50 snow layers that exchange mass and energy between them and at their upper and lower boundaries. Here, the model was used in a distributed geometry in a regular grid (Revuelto et al., 2018). There was no energy or mass transfer between the points, which indicates that wind drift, horizontal heat transfer and avalanches were not modeled. However, shading due to topography was considered in the incident shortwave radiation. We used the multiphysics version ESCROC-E1, which is an ensemble of 575 sets of parameterizations of eight physical processes implemented in the model (Lafaysse et al., 2017). The parameterization of the density of the new snow and of the compaction rate are expected to have the largest impact on HS. As in Cluzet et al. (2021), a set of 120 parameterizations was randomly drawn once and used for all WY and experiments.

The density and mass of each layer are prognostic variables in the model. Thus, assimilating HS can result in modifying the SWE, the density or both. The SMOD was defined as the end of the longest period with continuous snow cover. At each time step and for each grid point, the modeled median HS map was converted to an SCA map with a threshold determining the presence or lack of snow. The optimum HS threshold was chosen among six values in the 0.02 m-0.50 m range so that it minimizes the mean and standard deviation of the SMOD residual (SMOD Crocus minus SMOD Sentinel-2/Landsat 8). Based on these criteria, the optimal threshold was 0.20 m (Figure S1), which is close to the threshold of 0.15 m that maximizes the agreement between MODIS SCA (500 m resolution) and in situ HS in the Pyrenees (Gascoin et al., 2015).

The snowpack was simulated over five WY (WY 2014-2015 to WY 2018-2019) on a regular grid of points separated by 250 m with a 15 min time step (Figure 1). An ensemble of 120 simulations was obtained by stochastic perturbations of the SAFRAN reanalysis and the use of different physical parameterizations of the Crocus model (Lafaysse et al., 2017) (Figure 3). Once per hydrological year, an HS map was assimilated with the particle filter of the data assimilation scheme CrocO (Cluzet et al., 2021). The filter was applied independently to each grid point where observations were available using only the observation at that grid point, following the *rlocal* approach (Cluzet et al., 2021). The particle filter works in two steps. First, the ensemble members (i.e. particles) are assigned a weight which is proportional to their distance to the observation and is relative to the observation error. The observation error is assumed to be

normally distributed with a defined standard deviation. Then, the particles are resampled (i.e. eliminated or duplicated) based on their weight following Kitagawa (1996). Each particle results from a meteorological forcing and a parameterization of the model. The particle filter only resamples state vectors and has no influence on the forcing-model couples before or after the assimilation. Nevertheless, we compare the meteorological forcings and the model parameterizations associated with the particles selected by the filter (i.e. with assimilation) with the one of the ensemble without assimilation.

3.2. Simulation grid and boundary conditions

The topography of the simulation grid was the snow-free digital elevation model (DEM) calculated from the October 2014 Pléiades images. It was aggregated from its initial horizontal resolution (3 m) to the simulation grid resolution (250 m) with an average block filter. The soil and vegetation conditions were extracted at each grid point from the Harmonized World Soil Database (FAO/IIASA/ISRIC/ISS-CAS/JRC, 2012) and Ecoclimap-2 data sets (Faroux et al., 2013), respectively. The interaction between snowpack and forest was not accounted for because the implementation of this complex coupling in SURFEX-Crocus is still in progress and not sufficiently mature at the moment (Vincent et al., 2018) and because HS cannot be retrieved in forest with satellite photogrammetry. The soil state (temperature and water/ice content) was initialized with ten iterations of a one-year spin-up simulation with the meteorological conditions of WY 2014-2015. All grid points were snow free on the last day of the spin-up simulations.

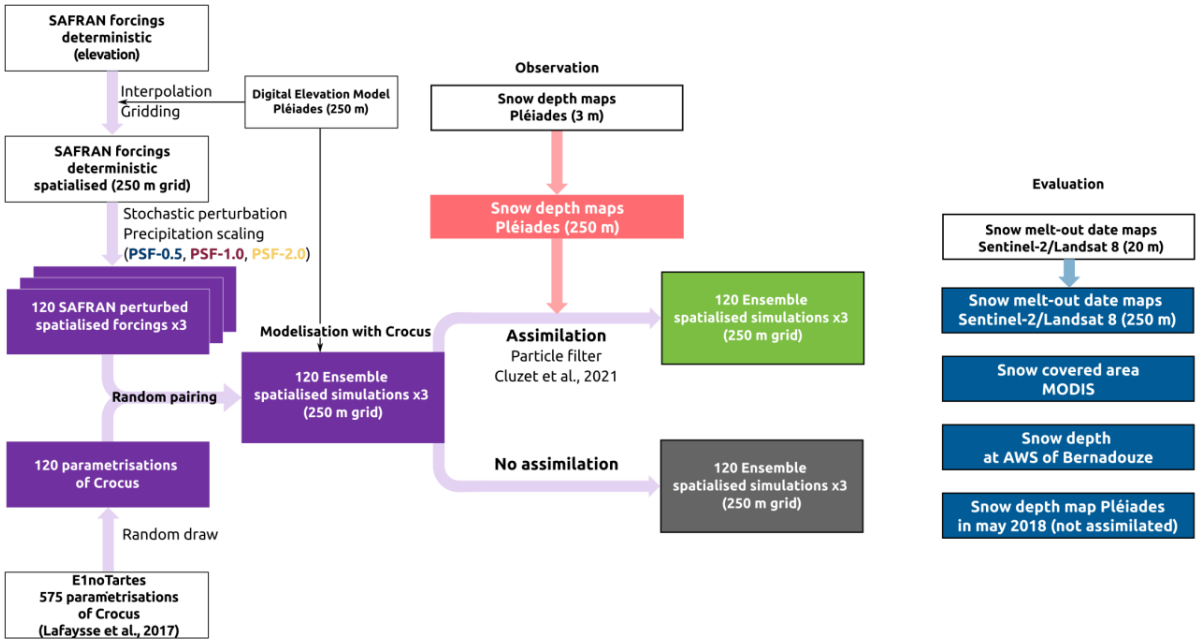

Figure 3. General setup of the assimilation experiments. Pléiades HS maps (pink box) are assimilated with a particle filter in Crocus ensemble simulation (purple box). The ensemble results from perturbation of the meteorological forcings and different physical parameterizations of the Crocus model (purple boxes left). The assimilation run (green box) is evaluated by comparison with the run without assimilation (grey box) and with independent dataset (blue boxes).

3.3. Satellite photogrammetric snow depth maps

A time series of seven triplets of stereoscopic images (i.e. three almost synchronous images of the study area from different points of view) was acquired by the Pléiades satellites between October 2014 and March 2019 (Gleyzes et al., 2012) (Table 1). The terrain was snow free in October 2014, which provided a reference snow-off observation. The other acquisitions occurred once every winter in March or April (snow-on) close to the date of peak SWE. During winter 2017-2018, two acquisitions were taken in February and May. Each acquisition provided a triplet (front, nadir, and back) of panchromatic images at a resolution of 0.5 m and a triplet of multispectral images (red, green, blue, and near-infrared) at a resolution of 2 m. The images were processed using a workflow that calculates a DEM from the panchromatic images and a land-

cover map from the multispectral images for each acquisition (Deschamps-Berger et al., 2020). The difference between a snow-on and snow-off DEM provided an elevation difference map for each snow-on acquisition. The land-cover map was labeled with the following classes: snow, snow in shade, stable terrain, stable terrain in shade, forest, forest in shade and lakes. The stable terrain is the area where no elevation changes are expected between the acquisitions (i.e., free of snow) and where the elevation is constant in the DEM (i.e., free of forest). The HS map was calculated by taking the elevation difference of snow-covered pixels and setting the HS to zero over stable terrain pixels. The HS maps had an initial horizontal resolution of 3 m and were aggregated using an average block filter of 250 m by 250 m centered on the simulation grid points. HS were set to no-data if more than 90% of the pixels were no-data. This means that more than 10^3 m² of HS are averaged, decreasing the error by a factor of two (Figure 10 in Deschamps-Berger et al. (2020)). No-data pixels correspond to portions of the panchromatic images that were saturated, covered with forest or with clouds. HS maps were also filtered to exclude HS values out of the [-0.5 m; 30 m] range, which can occur due to local artifacts in DEMs in shaded or forested areas in the snow-off DEM.

We defined a unique standard error for the measured HS, which is considered in the particle filter. The standard error of the HS at a resolution of 250 m is lower than the standard error at a resolution of 3 m due to the decrease in the random spatially-correlated error. A random error of 0.3 m was measured for a 250 m x 250 m averaging area at a mountainous site in California (Figure 10 in Deschamps-Berger et al., 2020). A systematic error of 0.2 m was also typically observed with similar data in several other studies (Table 4 in Deschamps-Berger et al., 2020). We added these two error estimates to consider the uncertainty of how error can be transferred from one site to another. Thus, the standard error of the HS at 250 m is 0.5 m.

3.4. Meteorological forcings

The meteorological variables needed as inputs in Crocus are air temperature, solid and liquid precipitation, near-surface specific humidity, direct and diffuse shortwave radiation, longwave radiation, and wind speed. The meteorological forcings were provided by the SAFRAN reanalysis (Vernay et al., 2021) at an hourly resolution. SAFRAN provides meteorological data

289 for different elevation levels at a 300 m resolution within predefined regions of homogeneous
290 climate of approximately 1000 km², the so-called "Couserans massif" in this study. The forcings
291 were interpolated on the simulation grid according to their elevation (Revuelto et al., 2018).
292 Solar radiation was projected according to local slopes and shading effects computed in
293 dedicated routines of the SURFEX platform as in Revuelto et al. (2018).

294 The initial gridded forcing was perturbed stochastically to produce ensembles of 120 forcings.
295 Perturbation of the forcings aims to generate an ensemble of forcings with a dispersion among
296 the forcings matching their uncertainty. The stochastic perturbation was spatially constant and
297 temporally correlated following an updated version of the Charrois et al. (2016) method (see
298 Text S1). Perturbation of each meteorological variable was defined by two parameters, its
299 amplitude and its temporal correlation. All variables were perturbed with the parameters defined
300 in Charrois et al. (2016) at the Col de Porte site (Alps), except for precipitation because we found
301 that the uncertainty of annual cumulative precipitation was severely underestimated by Charrois
302 et al. (2016). Therefore, the temporal correlation of precipitation was increased from 15 hours to
303 1500 hours. This increases the dispersion of the annual cumulative precipitation among the
304 forcings and of the resulting average HS among the simulations in a magnitude more
305 representative of the typical known errors for both variables. In addition, three different sets of
306 forcings were calculated with three spatially and temporally uniform precipitation scaling factors
307 (PSF) to emulate precipitation biases that are typically observed in global reanalyses (Beck et al.,
308 2019). The reference experiment was run with a PSF of 1.0 (referred to as PSF-1.0) and was
309 compared with experiments in which precipitation was halved (PSF-0.5) or doubled (PSF-2.0).
310

311 ### 3.5. Evaluation products and metrics

312 First, the impact of assimilation on the modeled snowpack was observed on the HS, SWE, bulk
313 density and runoff by comparison of the simulation with assimilation and the simulation without
314 assimilation. Then, the benefits of assimilation was measured by comparing the modeled HS
315 with the following independent observations:

316 - for WY 2017-2018 with a Pléiades HS map in May 2018, which was not assimilated

317 - a time series of HS at the Bernadouze AWS

318 - a time series of SCA derived from MODIS images

319 - a time series of SMOD maps calculated from Sentinel-2 and Landsat 8 images.

320 Note that we do not have observations of SWE or runoff on this area.

321 For each variable, *X*, describing the snowpack (i.e., HS, SWE, density, and runoff), a simulated
322 ensemble was characterized by its mean, the first and third quartiles and its dispersion. These
323 metrics were calculated for each time step (*t*) and each point of the grid (*i,j*). The mean is:

324 $$\overline{X(\imath,\jmath,t)} = \frac{1}{N}\sum_{n=1}^{N}\overline{X(\imath,\jmath,t,n)} \qquad (1)$$

325 where N is the size of the ensemble (N=120). The spread of the ensemble is

326 $$\sigma(i,j,t) = \sqrt{\frac{1}{N}\sum_{n=1}^{N}\left(X(i,j,t,n) - \overline{X(\imath,\jmath,t)}\right)^2} \qquad (2)$$

327 The mean is used to make a point-by-point comparison of the simulated ensemble with a
328 reference map (HS and SMOD). It is used to compute the absolute bias between the ensemble
329 and observation at a given point. However, it is not adapted to characterize the complete
330 distribution of the ensemble. The continuous ranked probability score (*CRPS*) is a probabilistic
331 score measuring the distance between the ensemble and observations (Hersbach, 2000). It
332 compares the cumulative distribution function of the ensemble, *Fens*, with the observation, *Fobs*:

333 $$CRPS(i,j,t) = \int_{-\infty}^{+\infty}[Fens(i,j,t,x) - Fobs(i,j,t,x)]^2\,dx \qquad (3)$$

334 where *Fobs* is a step function defined by the observation value *Xobs*:

$$Fobs(i,j,x) = 1 \;\; if x > Xobs \;;\; 0 \;\; otherwise$$

335 The higher the CRPS, the more the modeled ensemble is different from the observation. Thus,
336 the assimilation aims at reducing the CRPS of the model compared to independent observations.

337 If not specified, the metrics were spatially averaged over grid points where observations were
338 available. For the MODIS SCA and Bernadouze HS time series, the RMSE was calculated

between the modeled and observed variables from the assimilation date to the end of the WY. The spatial variability of the modeled and observed HS maps was measured with semivariance (Blöschl, 1999; Deems et al., 2006).

3.7. Snow melt-out date from Sentinel-2 and Landsat 8 images

We obtained every snow cover product available from the remote sensing products distribution platform Theia between September 2016 and September 2019 (Gascoin et al., 2019). These snow cover products were derived from Sentinel-2 and Landsat 8 images and provide a classification of the surface as snow, no snow or cloud (including cloud shadow) at 20 m (Sentinel-2) or 30 m (Landsat 8). Landsat 8 data were resampled to the Sentinel-2 20 m resolution grid by using nearest neighbor interpolation. When Sentinel-2 and Landsat 8 data were available on the same day, both products were merged by giving priority to Sentinel-2 on a pixel basis, i.e., Landsat 8 observations were used only if the Sentinel-2 pixel was classified as cloud. This time series was linearly interpolated along the time dimension to produce a daily, gap-free time series of snow absence and presence at a 20 m resolution between 1 September 2016 and 1 September 2019. Maps of the SMOD were calculated from the snow cover time series following the same definition as the simulated SMOD. The SMOD maps were aggregated with an average block filter of 250 m by 250 m centered on the simulation grid points. The SMOD was set to no-data if more than 90% of the initial pixel was covered with forest. The standard error of the SMOD measurement was estimated at 6 days based on the revisit time between successive acquisitions (~2.5 days) and the possible confusion with clouds.

3.8. Snow cover maps from MODIS

We used a collection of six Terra MODIS snow products (MOD10A1.006) to compute the SCA of the model domain. The snow cover fraction (SCF) of each MODIS pixel (approximately 500 m) was derived from the "Snow cover NDSI" field using the formulae of Salomonson and Appel (2004). Prior to computing the SCF, the missing values (approximately 50% of the data, mostly due to cloud cover) were linearly interpolated to generate a gap-free, daily time series as above with the Theia snow cover products. For every day between 1 September 2015 and 1 September 2019, a daily continuous SCA time series was thus obtained by summing the area-weighted average of the SCF of each pixel within the study domain.

368 ### 3.9. Bernadouze meteorological station

369 The Bernadouze automatic meteorological station is located in a clearing at 1420 m a.s.l. north of
370 the study area (42.80°N, 1.42°E, Figure 1). HS is measured bihourly with an acoustic sensor with
371 a centimetric accuracy (Gascoin & Fanise, 2018).

372 **Table 1.** Summary of the data used in this study.

373

Type	Source	Date	Horizontal resolution
Digital elevation model	Satellite photogrammetry (Pléiades)	2014-10-01	3 m
Snow depth map	Satellite photogrammetry (Pléiades)	2015-03-11	3 m
		2016-04-11	3 m
		2017-03-15	3 m
		2018-02-15	3 m
		2018-05-11	3 m
		2019-03-26	3 m
Snow melt-out date	Sentinel-2/Landsat 8 images	WY 2016-2017 WY 2017-2018 WY 2018-2019	20 m
Snow cover area	MODIS	all WY	500 m
Snow depth	Bernadouze AWS	all WY	

374

375

376 **4 Results**

377 4.1. Impact of the assimilation on the simulated snow depth on the assimilation date

378 Figure 4 shows the maps of the difference between the mean modeled HS and Pléiades HS
379 observations on all assimilation dates, for the different Precipitation Scaling Factor values (PSF).
380 Assimilation increased, on average, the modeled HS (PSF-0.5 and PSF-1.0) or decreased the
381 modeled HS (PSF-2.0) (Figure 4, Table S1). In all experiments and for all assimilation dates,
382 assimilation increased the similarity between the spatial distribution of the modeled and observed
383 HS, as expected. The semivariogram analysis indicates that the spatial variability of the modeled
384 HS was increased by the particle filter (Figure 5). The differences between the ensemble without
385 assimilation and the Pléiades observations were larger at high elevations for PSF-0.5 and PSF-
386 1.0 and rather homogeneous at all elevations for PSF-2.0 (Figure 6 and S2). The modeled HS
387 was largely inferior to observed HS in the southern part of the area prior to assimilation,
388 independent of the elevation for PSF-0.5 and PSF-1.0 (WY 2014-2015, WY 2016-2017, Figure
389 6). This difference was even observed in PSF-2.0 despite the HS being increased by the doubling
390 of precipitation. The mismatch between observed and modeled HS in WY 2018-2019 could be
391 related to spatially structured errors in the Pléiades HS map (see 5.5).

392 Figure 7 presents the evolution of the spatial average of the mean absolute difference between
393 the observations and the model, the ensemble spread, the CRPS and the Pearson correlation for
394 assimilated Pléiades observations (solid line). As expected, the distance between the assimilated
395 observations and the model, shown by the CRPS and the mean absolute difference, is always
396 reduced by the particle filter compared to the runs without assimilation. The CRPS and the mean
397 absolute bias reduction were larger for PSF-0.5 and PSF-2.0 without assimilation than for PSF-
398 1.0, but the values were reduced by the assimilation and close to each other for all experiments.
399 For all years and experiments, the Pearson correlation between the modeled and observed HS
400 increased to ~0.99 after assimilation.

401 4.2. Impact of the assimilation on the simulated SWE, density, and runoff

On the date of the assimilation, the assimilation of the HS maps had different impacts on the modeled bulk density and the SWE depending on the experiment (Figure 8). The increase (PSF-0.5 and PSF-1.0) and decrease (PSF-2.0) in HS were associated with similar modifications of the SWE. Density was also modified to a lesser extent, typically +- 25 kg m3. Density was diminished for PSF-0.5 and some WY of PSF-1.0. Conversely, density was increased for PSF-2.0.

The change in SWE on the date of the assimilation also resulted in modification of the melt runoff amplitude and duration throughout the end of the snow season (Figure S4). Total melt runoff increased from 20% to 30% for PSF-0.5, by 10% or less for PSF-1.0 and decreased by 10% or less for PSF-2.0. The end of the melt period was extended by up to 10 days for PSF-0.5 and not modified for PSF-2.0.

4.3 Selection of the particles based on their meteorological forcing and their model physical parameterization

The HS of ensemble members that are selected by the particle filter may be more appropriate due to their meteorological forcing, their physical version of the Crocus model, or both. Figure 9 shows the mean precipitation until the assimilation date of WY 2014-2015 associated with all the particles of the ensemble (gray) and associated with the particles selected by the filter (green). Particles with higher precipitation rates were selected for PSF-0.5 and PSF-1.0 in agreement with the observed increase in SWE due to assimilation for these two experiments. Particles with lower precipitation rates were selected for PSF-2.0, again in agreement with the associated SWE reduction. Distribution of the other meteorological variables was not modified by assimilation.

Figure 10 shows the versions of the compaction modeling in Crocus associated with all the particles of the ensemble with and without assimilation. No version of the compaction was excluded by the assimilation, but some were preferentially selected. The compaction version from Anderson (1976) was preferred at the expense of the version from Teufelsbauer (2011) in the PSF-0.5. The opposite preferential selection occurred in PSF-2.0. No clear impact of

assimilation was observed for PSF-1.0 or for other physical laws impacting snowpack density (i.e., density of fresh snow and snow grain metamorphism).

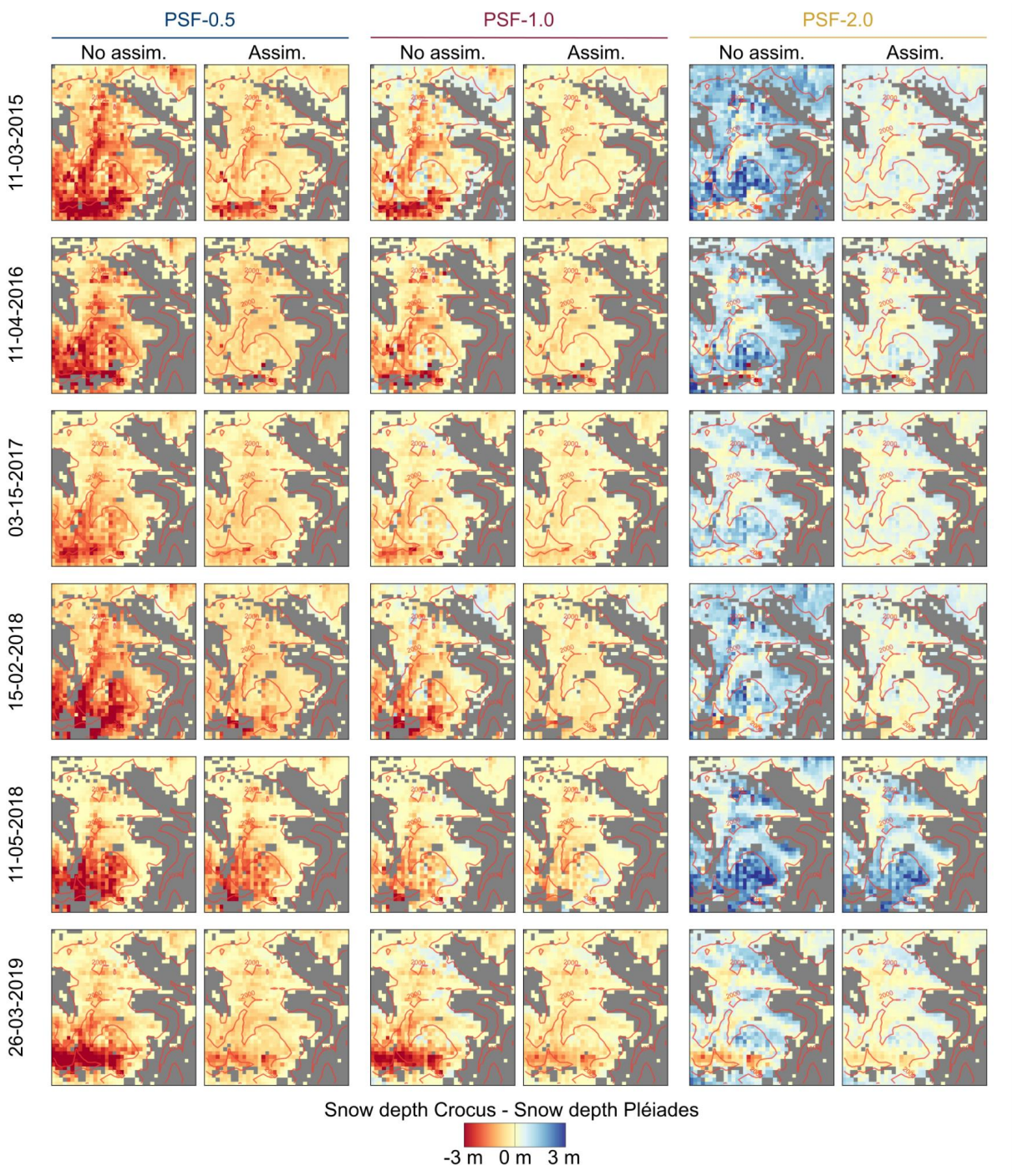

Figure 4. Differences of snow depth maps (Crocus minus Pléiades) without assimilation (left column for a given PSF) and with assimilation (right column for a given PSF). The rows show

434 the different acquisition dates. The differences are always smaller in the assimilation run, even
435 on 11 May 2018, 85 days after the assimilation date.

436

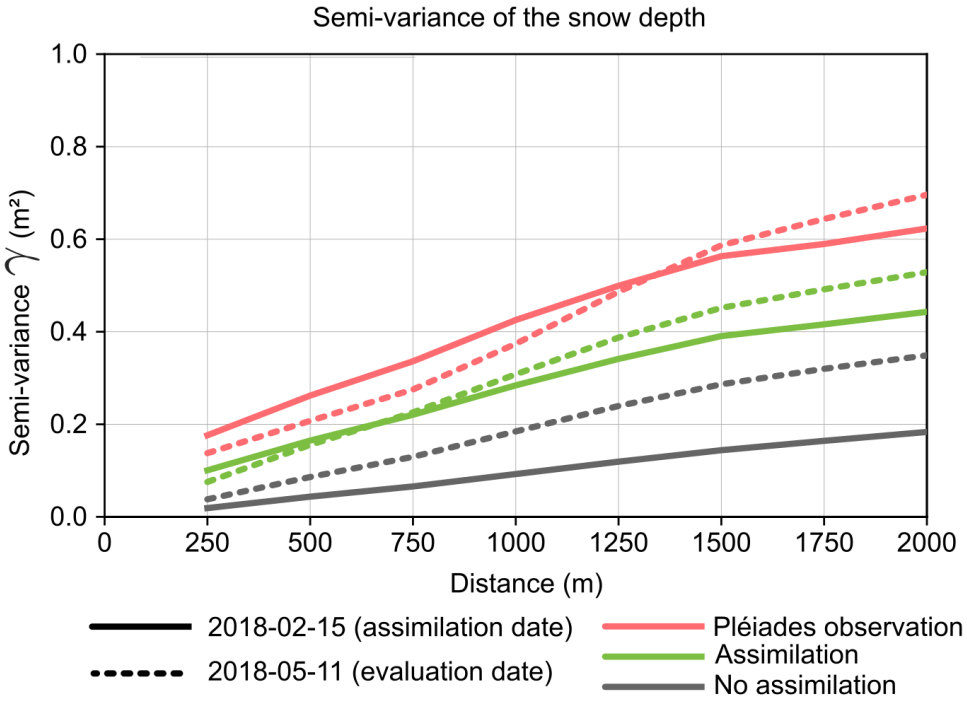

437

438 **Figure 5.** Semi-variogram of the snow depth modeled without assimilation (grey), with
439 assimilation (green) and in the Pléiades snow depth maps. The thick solid lines show the 15
440 February 2018 semi-variance (assimilation date) and the thick dashed lines show the 11 May
441 2018 semi-variance (evaluation date). The assimilation increased the spatial variability of the
442 modeled HS at the assimilation date. This improvement remains 85 days after the assimilation on
443 11 May 2018.

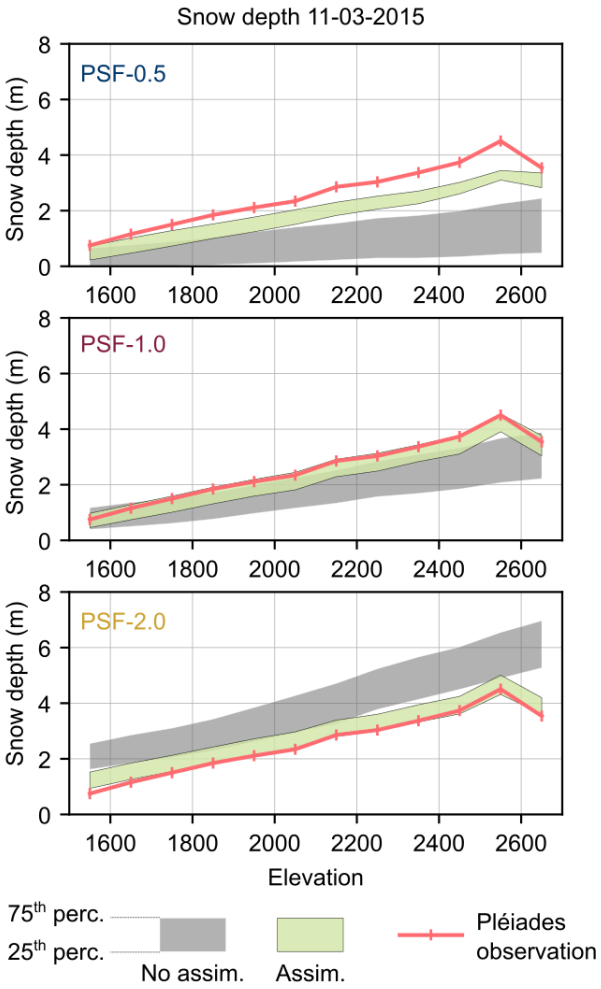

Figure 6. Envelopes of the snow depth ensemble without assimilation (grey) and with assimilation (green) as a function of elevation. The envelope shows the first and third quartile of the ensemble distribution. The rows show the three precipitation scaling experiments, from top to bottom: PSF-0.5, PSF-1.0, PSF-2.0. The snow depth measured with Pléiades (red) is identical in all plots.

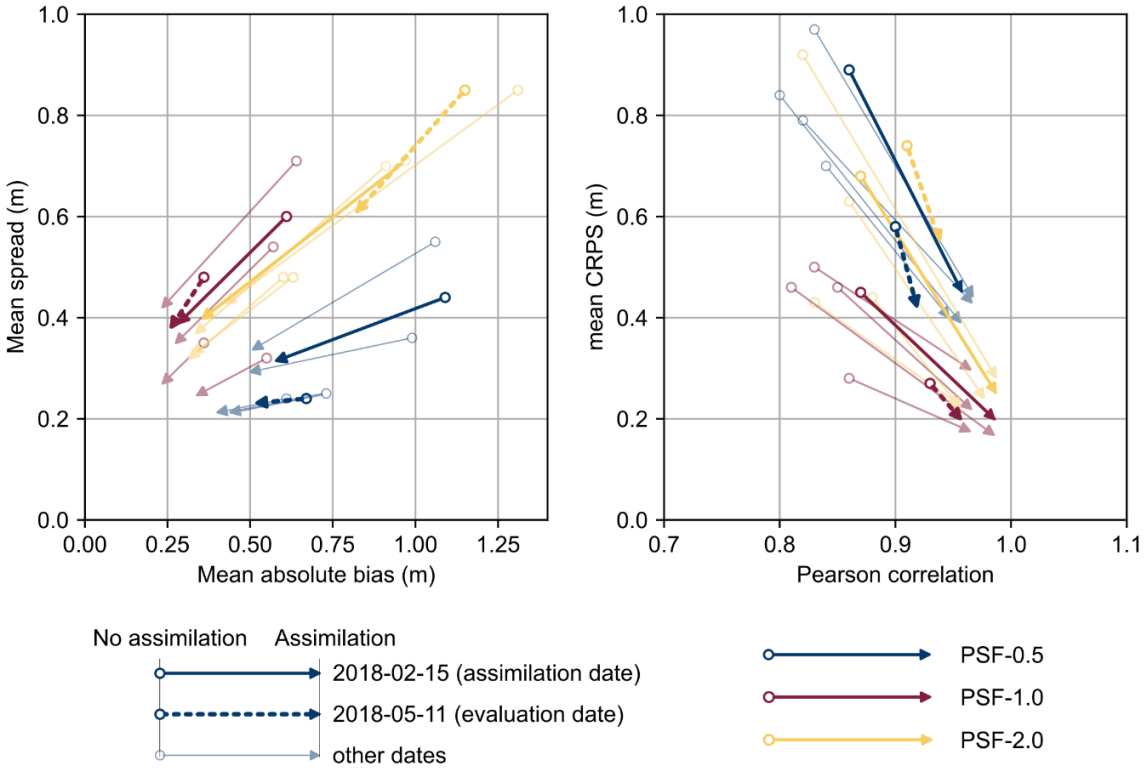

Figure 7. Impact of the assimilation on the modeled snow depth at the assimilation date (solid line) and on the evaluation date (dashed line) compared to Pléiades snow depth maps. Left plot shows the ensemble spread and the mean absolute error. Right plot shows the CRPS and the Pearson correlation. Each arrow shows the statistic for a single date with the metrics without assimilation at the base of the arrow and the metrics with assimilation at the head of the arrow. February and May 2018 arrows are in full colors while other dates are slightly transparent. The arrow color shows the precipitation scaling factor. The assimilation reduced the spread of the ensemble, the bias between the modeled HS and the observation, the mean CRPS and increased the correlation between the modeled HS and the observation. This is expected at the assimilation date but the fact that it subsists on 11 May 2018 shows the long-lasting benefit of the assimilation.

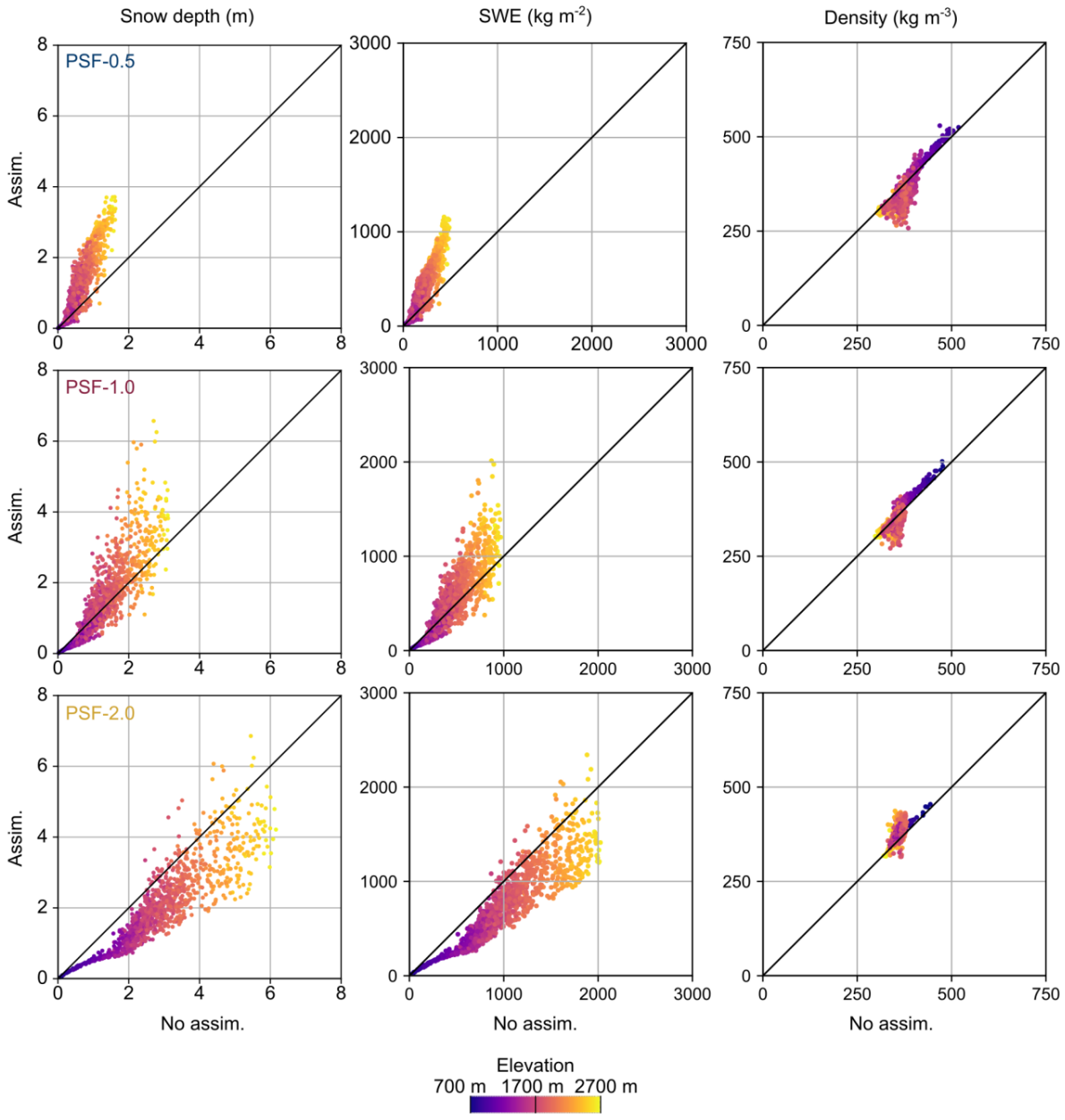

Figure 8. Impact of the particle filter on snow depth (left), SWE (middle) and density (right) on 11 March 2015 (assimilation date). Each dot represents the mean value of a simulation grid point with the color showing the elevation of the point. The rows show the different precipitation scaling experiments, from top to bottom: PSF-0.5, PSF-1.0, PSF-2.0.

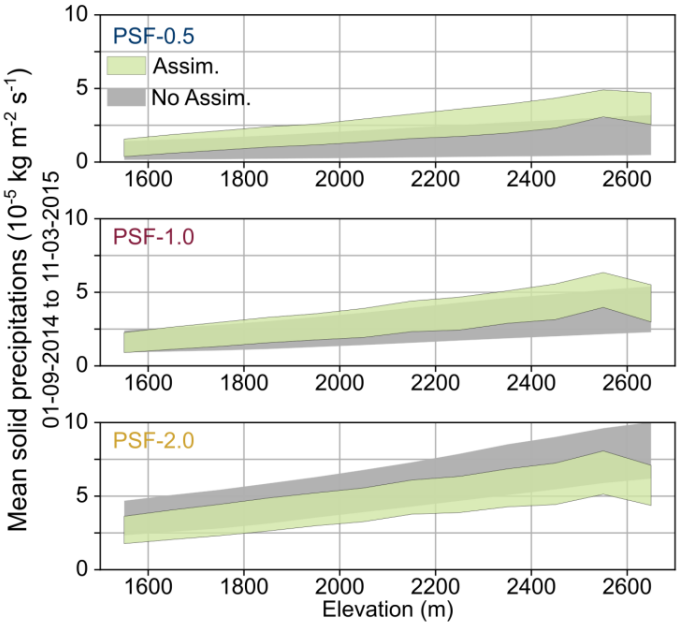

Figure 9. Solid precipitation rate per elevation between 1 September 2014 and 11 March 2015 (assimilation date). Green envelope shows the precipitation of the particles selected by the assimilation (the first and third quartile). Grey envelope shows the precipitation of all the particles (i.e. no assimilation). The assimilation selected members with mean precipitations compensating the bias introduced by PSF-0.5 and PSF-2.0.

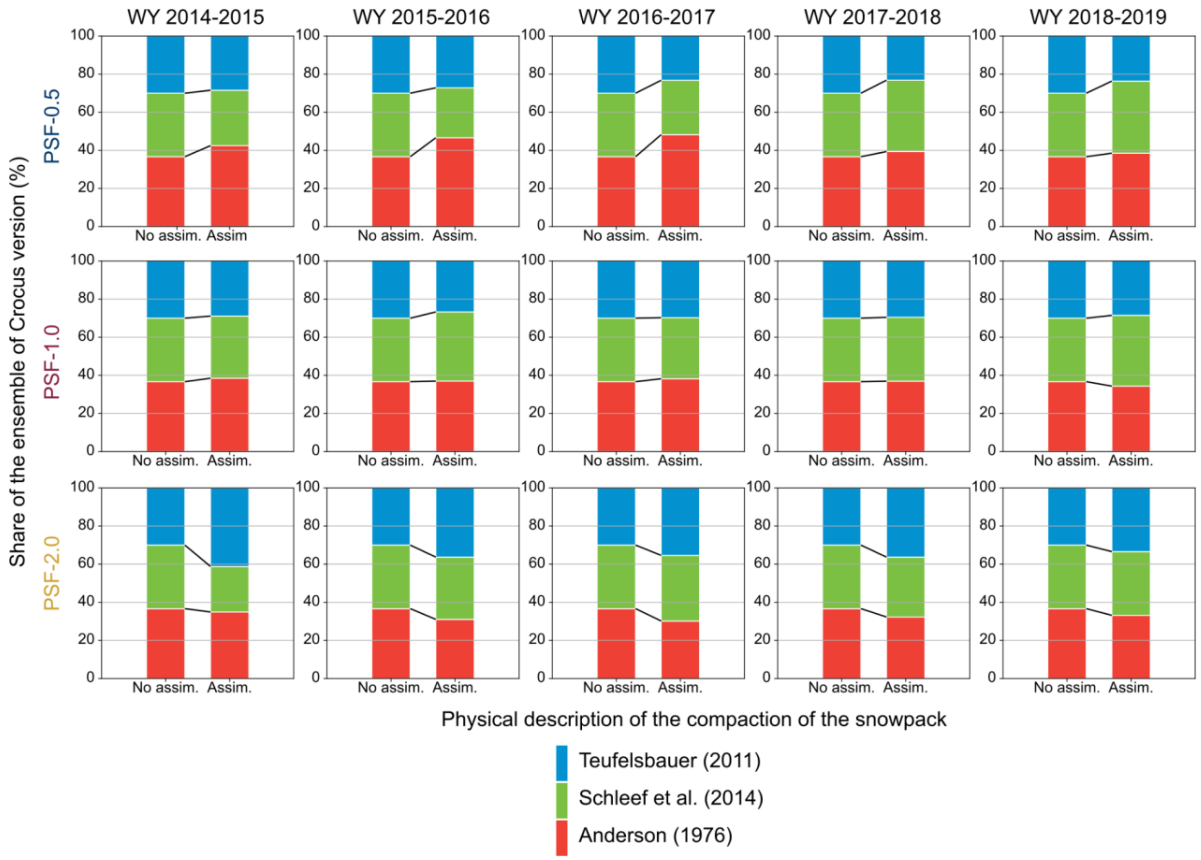

Figure 10. Distribution of the physical parameterizations of the snowpack compaction of all the particles (i.e. no assimilation, left bar) or of the particles selected by the assimilation (right bar). Each column shows the distribution for a WY and each row shows the distribution for the precipitation scaling experiments, from top to bottom: PSF-0.5, PSF-1.0, PSF-2.0. The assimilation selected and eliminated preferentially some physical parameterizations of the PSF-0.5 and PSF-2.0 experiments.

4.4. Independent evaluation of the impact of assimilation

A Pléiades HS observation is available on 11 May 2018, 85 days after the assimilation date of 15 February 2018, enabling us to assess the impact of the assimilation on the modeled snowpack with independent data. The mean bias and spread of the ensemble were reduced in the assimilation run on this date (dashed arrows in Figure 7). The mean CRPS was smaller in May in the assimilation run than without assimilation for all elevation levels (Figure 11). The spatial variability introduced by assimilation was also conserved in May (dashed line in Figure 5).

493 HS measured at the Bernadouze AWS was 1.17 m and 0.82 m on the assimilation dates of WY
494 2014-2015 and WY 2017-2018, respectively (Figure S5). It was null or close to null (i.e., <0.3
495 m) on all other assimilation dates both in Pléiades and at the AWS. HS at the closest grid point
496 was improved (i.e., decreased) from ~0.3 m to 0.5 m by assimilation for PSF-2.0. It was slightly
497 improved by ~0.1 m (i.e., increased) for PSF-0.5 for WY 2014-2015 and WY 2017-2018, which
498 were WY with the thickest snowpack during the study period. The impact was null or weak for
499 other assimilation dates of PSF-0.5 and PSF-1.0 due to the lack of snow or good agreement
500 between the model and Pléiades observation prior to assimilation.

501 After assimilation, the modeled SMOD was delayed by typically 15 days for PSF-0.5 compared
502 with the modeled SMOD without assimilation. This improved the modeled SMOD by the same
503 duration, as shown by the map of the difference between modeled and SMOD observed by
504 Sentinel-2/Landsat 8 (Figure 12). Conversely, the modeled SMOD was advanced and generally
505 improved by approximately 5 days for PSF-2.0. However, assimilation locally degraded the
506 modeled SMOD in the southern part of the zone in WY 2017-2018 and WY 2018-2019. The
507 impact of assimilation on the SMOD was null on average for PSF-1.0. The modeled SCA was
508 improved by assimilation compared with MODIS SCA (Figure S6). The RMSE of SCA was
509 reduced by ~20% for PSF-1.0 and PSF-2.0, and ~30% for PSF-0.5 (not shown).

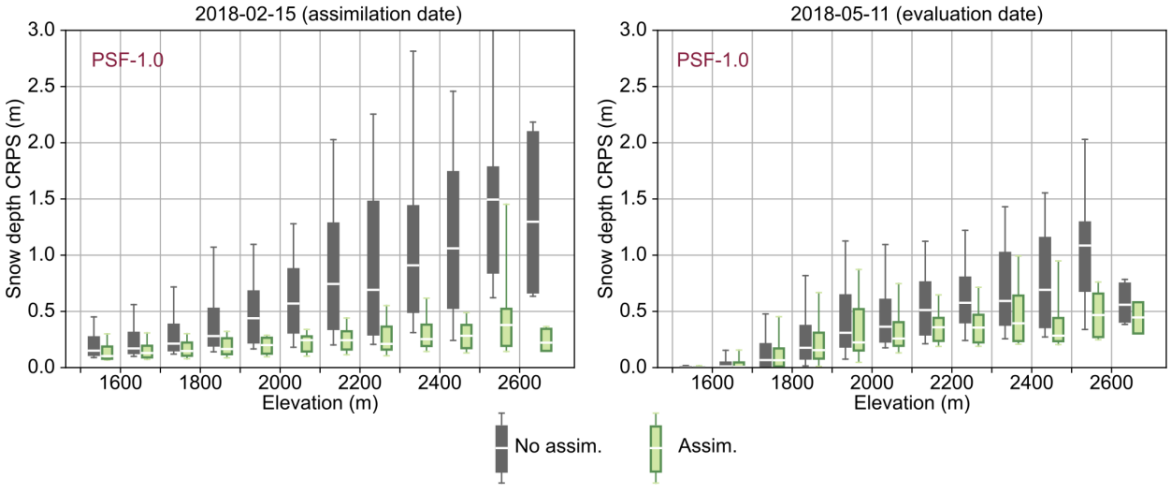

510

511 **Figure 11.** Distribution of the snow depth CRPS against elevation on 15 February 2018
512 (assimilation date) and 85 days later on 11 May 2018 (evaluation date). The CRPS is calculated
513 from the modeled snow depth without assimilation (grey), with assimilation (green) and a

514 Pléiades snow depth map. Reduction of the CRPS is visible at both the assimilation date and, to a
515 smaller extent, at the evaluation date.

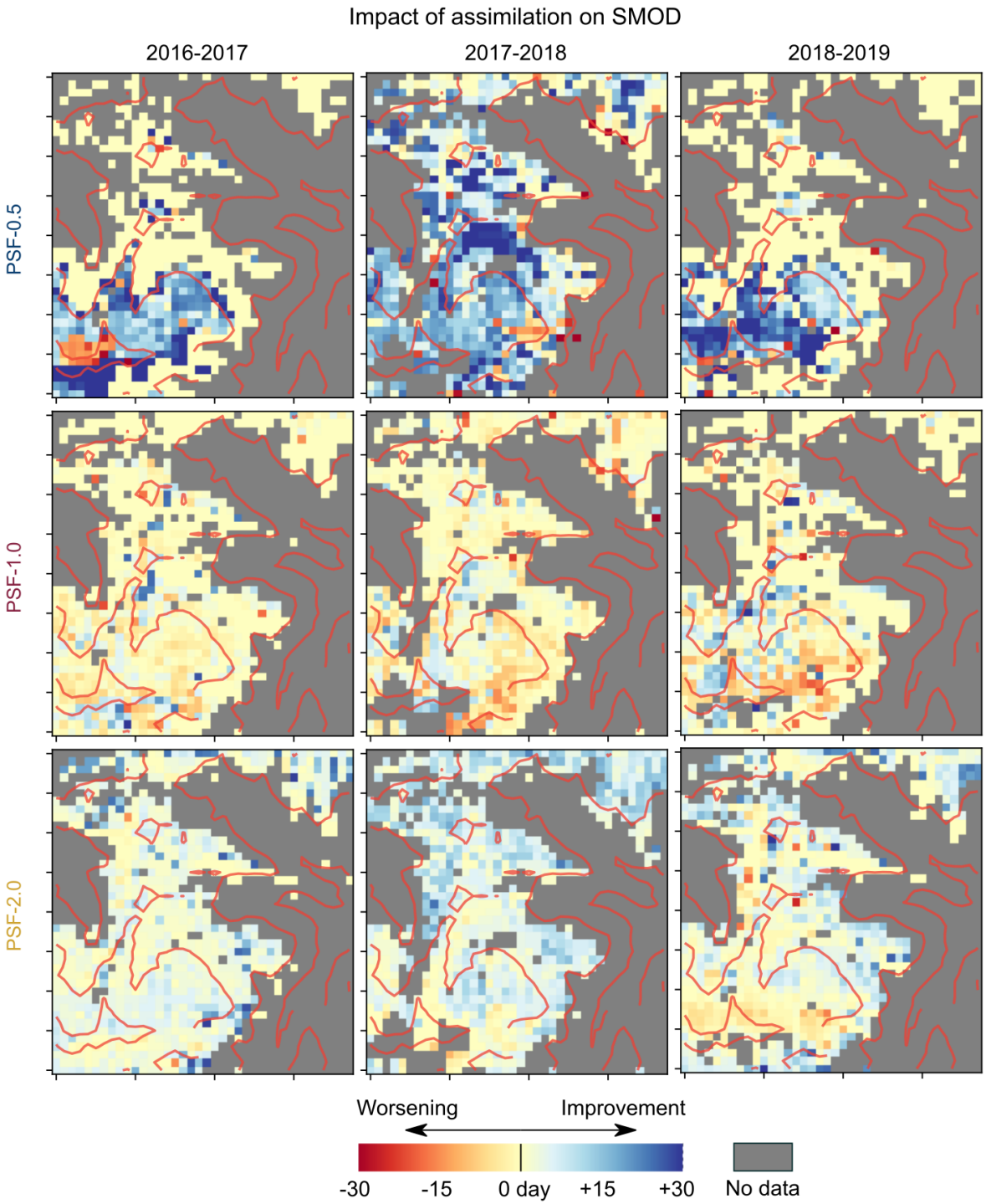

516

Figure 12. Impact of the assimilation on the modeled SMOD in days. Blue areas show improvement of the modeled SMOD while red areas show worsening of the modeled SMOD by the assimilation. Modeled SMOD in the yellow areas was not modified by the assimilation. SMOD was improved by the assimilation in PSF-0.5 and to a lesser extent in PSF-2.0.

5 Discussion

5.1. Correction of errors in the meteorological forcings

The mean precipitation of the particle selected by the particle filter differed from the mean precipitation of all particles (Figure 9). This was observed in PSF-0.5 and PSF-2.0 which emulate bias in precipitation observed in global reanalyses (Beck et al., 2019) and also in PSF-1.0 which provides a reference run to compare HS observations from Pléiades with those from the SAFRAN-Crocus chain. HS was underestimated in PSF-1.0 without assimilation of snow observations, especially at elevations above 2000 m a.s.l. The discrepancy was typically 10% to 20%. This bias had the same sign and similar magnitude than those previously reported by comparing SAFRAN-Crocus simulations with HS measurements in this part of the Pyrenees (Quéno et al., 2016). The strong precipitation gradient with elevation is difficult to reproduce for an analysis system without any observation at high elevation, explaining the increasing bias of HS with elevation (Vionnet et al., 2019). As the assimilation improved the modeled HS (Figure 4, 7, and 11), SMOD (Figure 12), and SCA (Figure S5) in PSF-0.5 and PSF-2.0, we conclude that errors in precipitation can be reduced by the assimilation of Pléiades HS in case of large bias. In case of smaller bias (e.g. PSF-1.0), we conclude that the assimilation of Pléiades HS map benefits by improving the modeled spatial variability of HS (Figure 5).

The assimilation had no clear impact on the other meteorological variables. This likely results from the short correlation time of the applied perturbation, which did not sufficiently differentiate the particles. A short correlation time of the perturbation (i.e., 15 h) results in an ensemble of forcings with a random distribution at each time step but a similar yearly mean. Smyth et al. (2019) found that the perturbation of radiative forcing and of precipitation produced assimilation results similar to those of the perturbation of precipitation only. Increasing the correlation time of the perturbation of the temperature could be relevant in evaluating the impact

of a large bias in temperature, as it controls the precipitation phase partition during precipitation events.

5.2 Correction of errors in the physical parameterization

Density of the snowpack was also modified by assimilation. Density could be modified as a consequence of SWE modification; more SWE due to more precipitation should lead to more compaction and denser snowpack on average. However, the sign of density modification was not consistent with this hypothesis (e.g. PSF-0.5 in Figure 8). The densification law from Anderson (1976) favored in PSF-0.5 leads to slower densification than the law from Teufelsbauer (2011), depreciated by the assimilation. This indicates that the increase in HS for PSF-0.5 also resulted from a slower densification and the decrease in HS for PSF-2.0, resulted from a faster densification. This is not necessarily a good reason, as the bias of the HS is related to precipitation errors by construction in the PSF-0.5 and PSF-2.0 experiments.

The same phenomenon was observed when assimilating synthetic punctual HS in a two-layer model (Smyth et al., 2019). While Smyth et al. (2019) concluded that the modeled density was improved by assimilation thanks to SWE and HS measurements, we lack in situ measurements to perform similar evaluations. Our experiments suggest that assimilation can compensate for meteorological errors by the selection of different physical parameterizations. As a result, an improvement of the simulated SWE can not be systematically guaranteed through HS assimilation. Including different observed variables in the assimilation scheme should help avoid these equifinality issues in the future.

5.3. Evolution of the snowpack after the assimilation date

Satellite-based data (Pléiades, MODIS, Sentinel-2, and Landsat 8) provided independent spatial information to evaluate assimilation performance (Figure 4, 5, 7, 11, and 12). Impact of assimilation on the SMOD was only evident for PSF-0.5 and PSF-2.0 because the modeled

572 SMOD was largely degraded before the assimilation and the HS increment due to assimilation
573 was large. No positive impact of assimilation in PSF-1.0 was visible in the SMOD comparison,
574 probably because the limited HS assimilation increments likely resulted in SMOD changes that
575 were too small to be captured by the daily to biweekly resolution of the Sentinel-2/Landsat 8
576 SMOD products. In addition, several physical processes shaping the snowpack between the
577 assimilation date and SMOD are not taken into account in this version of Crocus (e.g., wind drift,
578 avalanche deposits, multiple reflections from surrounding surfaces, and light-absorbing
579 particles). For instance, the impact of light-absorbing particles was considered through the
580 decrease in visible albedo with snow age, and the parameterization was calibrated at the Col de
581 Porte site in the Alps (Brun et al., 1992). This does not represent the spatial and temporal
582 variability of the light-absorbing particles present in the modeled snowpack. The TARTES
583 module, which explicitly represents the impact of the light-absorbing particles, was not used
584 because it requires many more computational resources and additional forcing data (Tuzet et al.,
585 2017). The explicit modeling of the light-absorbing particles leads to faster melting and a ~6-day
586 advance of the SMOD in this region compared with the Crocus version used here (Réveillet et
587 al., in review). The impact is larger at high elevations and could partially explain the local
588 worsening of the modeled SMOD at high elevations in PSF-1.0 and PSF-2.0. In this area,
589 assimilation increased the HS, which delayed the SMOD, but the SMOD was already
590 overestimated without assimilation.

591

592 ### 5.4. Perspective on the assimilation scheme

593 Ensemble simulations provide an estimate of the uncertainty of the modeled variables of
594 interest (e.g. SWE, density) by the way of the ensemble spread. In theory, assimilation should
595 reduce the spread to the magnitude of observation error but should not underestimate the residual
596 uncertainty by a too selective particle filter leading to ensemble collapse (i.e., selection of a
597 single particle). Here, assimilation reduced the spread of the ensemble of modeled HS in the
598 range to the observation error (Figure 7). This suggests that the spread of the ensemble of HS
599 prior to assimilation, the bias between the ensemble prior to assimilation and observation, and
600 the observation error were consistent. However, assimilation did not modify the ensemble for

601 points at low elevation for PSF-0.5, where all members of the ensemble had no snow. The
602 multiplicative perturbation of precipitation used here cannot produce an ensemble of the HS with
603 a sufficiently large spread where snow falls are low and snowpack is thin. A way to address this
604 issue would be to introduce a spatially variable perturbation of precipitation and to increase the
605 perturbation amplitude in areas of thin snowpacks (i.e., low elevation and strong wind erosion)
606 or to use additive perturbation of the precipitation (Magnusson et al., 2017).

607 5.5. Snow depth mapping methods

608 Higher resolution and more accurate products can be generated from airborne surveys (Brauchli
609 et al., 2017; Hedrick et al., 2018). The higher accuracy reached with airborne lidar or
610 photogrammetry reduces the need to aggregate HS maps and allows higher resolution
611 simulations. In particular, satellite photogrammetry DEM can suffer from errors in the estimation
612 of the satellite attitude which results in erroneous undulations in the HS maps, so called “jitter”
613 (Deschamps-Berger et al., 2020). The magnitude and the spatial distribution of the difference
614 between modeled and observed HS on 26 March 2019 suggest that the corresponding winter
615 DEM is affected by jitter. The jitter is a spatially structured error whose magnitude depends on
616 the image and varies within an image. The largest negative anomaly of modeled HS in the south
617 of the study site on 26 March 2019 is likely due to an undulation of large amplitude. To our
618 knowledge, there is no way to correct for jitter without significant areas of stable terrain which is
619 the case here. Despite this error in the assimilated HS, assimilation improved the modeled
620 SMOD for PSF-0.5 but notably degraded the modeled SMOD in the south for PSF-2.0, where
621 the error due to jitter is believed to be the largest. Despite these errors, the strong asset of satellite
622 photogrammetry is the ability to acquire images in any place of the globe. The typical coverage
623 of a Pleiades image (20 km by 20 km) is too small to cover a whole mountain range like airborne
624 methods could do (Painter et al., 2015). It remains much larger than UAV or terrestrial based
625 methods (Eberhardt et al., 2020).

626

627 5.6. Comparison to existing studies

Our results are in line with previous studies which concluded on the improvement of the modeled spatial distribution of the HS through assimilation of a single HS map, with other assimilation method, data source, data frequency and snowpack model (e.g. Revuelto et al., 2016; Brauchli et al, 2017; Hedrick et al., 2018; Margulis et al., 2019; Shaw et al., 2020). The observed improvement 85 days after the assimilation date in WY 2017-2018 is consistent with the persistence of reduced error up to 100 days after the assimilation date in simulations weighted with a particle batch smoother (Margulis et al., 2019). Our study confirms the experimental results of Smyth et al. (2020) who found that HS measurements with uncertainty of ~0.5 m, typical of satellite photogrammetry, are sufficient to significantly improve snowpack simulations in mountainous regions.

The assimilation date of a single HS map is often found to be optimal close to peak SWE for SWE estimation during the melt period (Brauchli et al., 2017; Hedrick et al., 2018; Margulis et al., 2019). The assimilation of an HS map acquired 50 days after peak SWE was less beneficial (Margulis et al., 2019). Here, the assimilation date was close to the basin peak SWE for WY 2014-2015, WY 2015-2016, and WY 2016-2017 but was ~40 days prior to the peak in WY 2017-2018 and ~50 days after the peak in WY 2018-2019. A third of the peak SWE mass accumulated after the assimilation date for WY 2017-2018, and a quarter was lost before the assimilation date for WY 2018-2019. However, the impact of assimilation on the SMOD (Figure 12) was similar for all WYs despite variable assimilation dates. This suggests that assimilation can be beneficial even with a single observation more than a month before or after the peak SWE.

6 Conclusion

Assimilation of a single HS map each year measured with satellite photogrammetry improved simulation of the snowpack based on comparison of the modeled HS with an independent HS map, independent satellite-derived maps of the SMOD and SCA. Assimilation corrected erroneous precipitation gradients and partially compensated for processes lacking in the model (e.g., wind redistribution) which improved the spatial distribution of modeled HS. The relatively high standard error of the HS measurements (~0.70 m at a 3 m resolution) compared with other remote sensing methods (e.g., drone or airborne) was reduced by aggregating the HS map at a

250 m resolution. Further work may evaluate the impact of assimilating HS maps from satellite photogrammetry at higher resolutions (<250 m) to represent smaller-scale variability. Cross validation dataset (airborne or terrestrial laser scan) would ease the measurement of the impact of assimilation of satellite snow depth maps. The use of satellite photogrammetry is currently limited by the footprint of the images (20 km x 20 km for Pléiades) and jitter errors. Variants of the particle filter, could partly overcome these limitation by propagating information into surrounding areas or erroneous areas by following correlation patterns in the ensemble (Cluzet et al., 2021). Although it may be better constrained in the future by complementary assimilation variables, the point-by-point particle filter used in this study already proved to be efficient and should be easily transferable to other study sites. These results and the possibility of using the particle filter several times per season when a new observation is available (sequential particle filter) combined with meteorological forecasts suggest that this scheme is well suited to operational applications (avalanche or flood forecasting). Assimilation had the largest impact on simulations with degraded meteorological forcings, which are representative of global reanalyses products. Combining satellite-derived snow depth observations, snowpack modeling and globally available forcings may especially allow an improved estimation of the snow cover properties in unmonitored mountain catchments (e.g., the Himalayas, Andes, and polar mountain ranges).

Acknowledgments

This work has been supported by the CNES Tosca (APR MIOSOTIS) and the Programme National de Télédétection Spatiale (PNTS; grant no. PNTS-2018-4). This work was cofunded by the LabEx DRIIHM, French program "Investissements d'Avenir" (ANR-11-LABX-0010) which is managed by the ANR (Observatoire Homme Milieu Pyrénées Haut Vicdessos). M.D. was partially funded by ANR JCJC EBONI. Marie Dumont has received funding from the European Research Council (ERC) under the European Union's Horizon 2020 research and innovation programme (grant agreement no. 949516, IVORI). CNRM/CEN is part of Labex OSUG@2020. Bernadouze weather station is supported by the Observatoire Spatial Régional (CNRS-INSU) and the Observatoire Homme Milieu (CNRS-INEE). Thanks to R. Marti and B. Pirletta for the pictures in figure 3. We thank Laura Sourp for useful discussions on the HS maps accuracy.

Data

The Pléiades images were obtained through DINAMIS (Dispositif Institutionnel National d'Approvisionnement Mutualisé en Imagerie Spatiale) which allows cost-less Pléiades acquisition for French research institutions. Otherwise Pléiades images can be ordered (i) at reduced cost for European researchers also via DINAMIS or (ii) via Airbus Defense and Space for non-EU researchers. The Pleiades snow depth maps used in this study are available at https://doi.org/10.5281/zenodo.4707494. Meteorological forcings are available at https://doi.org/10.25326/37 (version 2019 was used in this study).

Code

References

Anderson, E. (1976). *A point energy and mass balance model of a snow cover, NOAA Technical Report NWS 19.*

Andreadis, K. M., & Lettenmaier, D. P. (2006). Assimilating remotely sensed snow observations into a macroscale hydrology model. *Advances in Water Resources*, *29*, 872–886. https://doi.org/10.1016/j.advwatres.2005.08.004

Baba, M. W., Gascoin, S., Jarlan, L., Simonneaux, V., & Hanich, L. (2018). Variations of the snow water equivalent in the ourika catchment (Morocco) over 2000-2018 using downscaled MERRA-2 data. *Water (Switzerland)*, *10*(9). https://doi.org/10.3390/w10091120

Bard, A., Renard, B., Lang, M., Giuntoli, I., Korck, J., Volken, D., Koboltschnig, G., & Janz, M. (2015). Trends in the hydrologic regime of Alpine rivers. *Journal of Hydrology*, *529*, 1823–1837. https://doi.org/10.1016/j.jhydrol.2015.07.052

Barry, R. G. (2008). *Mountain weather and climate*. Cambridge University Press.

Beck, H. E., Pan, M., Roy, T., Weedon, G. P., Pappenberger, F., Dijk, A. I. J. M. Van, Huffman, G. J., Adler, R. F., & Wood, E. F. (2019). Daily evaluation of 26 precipitation datasets using Stage-IV gauge-radar data for the CONUS. *Hydrology and Earth System Sciences*, *23*, 207–224. https://doi.org/10.5194/hess-23-207-2019

Blöschl, G. (1999). Scaling issues in snow hydrology. *Hydrological Processes*, *13*(January), 2149–2175. https://doi.org/10.1002/(SICI)1099-1085(199910)13:14/15<2149::AID-

719 HYP847>3.0.CO;2-8

720 Brauchli, T., Trujillo, E., Huwald, H., & Lehning, M. (2017). Influence of Slope-Scale Snowmelt
721 on Catchment Response Simulated With the *Alpine3D* Model. *Water Resources Research*,
722 1–17. https://doi.org/10.1002/2017WR021278

723 Brun, E., David, P., Sudul, M., & Brunot, G. (1992). A numerical model to simulate snow-cover
724 stratigraphy for operational avalanche forecasting. *Journal of Glaciology*, *38*(128), 13–22.
725 https://doi.org/10.1017/S0022143000009552

726 Charrois, L., Cosme, E., Dumont, M., Lafaysse, M., Morin, S., & Libois, Q. (2016). On the
727 assimilation of optical reflectances and snow depth observations into a detailed snowpack
728 model. *The Cryosphere*, *10*, 1021–1038. https://doi.org/10.5194/tc-10-1021-2016

729 Choler, P. (2018). Perspectives in Plant Ecology , Evolution and Systematics Winter soil
730 temperature dependence of alpine plant distribution : Implications for anticipating
731 vegetation changes under a warming climate. *Perspectives in Plant Ecology, Evolution and*
732 *Systematics*, *30*(November 2017), 6–15. https://doi.org/10.1016/j.ppees.2017.11.002

733 Cluzet, B., Lafaysse, M., Cosme, E., Albergel, C., & Meunier, L. (2021). CrocO _ v1 . 0 : a
734 particle filter to assimilate snowpack observations in a spatialised framework. *Geoscientific*
735 *Model Development*, *14*, 1595–1614. https://doi.org/10.5194/gmd-14-1595-2021

736 Dedieu, J., Carlson, B. Z., Bigot, S., & Sirguey, P. (2016). On the Importance of High-
737 Resolution Time Series of Optical Imagery for Quantifying the Effects of Snow Cover
738 Duration on Alpine Plant Habitat. *Remote Sensing*, *8*. https://doi.org/10.3390/rs8060481

739 Deems, J. S., Fassnacht, S. R., & Elder, K. J. (2006). Fractal Distribution of Snow Depth from
740 Lidar Data. *Journal of Hydrometeorology*, *7*(2), 285–297.
741 https://doi.org/10.1175/JHM487.1

742 Deems, J. S., Painter, T. H., & Finnegan, D. C. (2013). Lidar measurement of snow depth : a
743 review. *59*(215), 467–479. https://doi.org/10.3189/2013JoG12J154

744 Deschamps-Berger, C., Gascoin, S., Berthier, E., Deems, J., & Gutmann, E. (2020). Snow depth
745 mapping from stereo satellite imagery in mountainous terrain : evaluation using airborne
746 laser-scanning data. *The Cryosphere*, 2925–2940. https://doi.org/10.5194/tc-14-2925-2020

747 Dozier, J., Bair, E. H., & Davis, R. E. (2016). Estimating the spatial distribution of snow water
748 equivalent in the world's mountains. *Wiley Interdisciplinary Reviews: Water*, *3*(3), 461–
749 474. https://doi.org/10.1002/wat2.1140

750 Dumont, M., Durand, Y., Arnaud, Y., & Six, D. (2012). Variational assimilation of albedo in a
751 snowpack model and reconstruction of the spatial mass-balance distribution of an alpine
752 glacier. *Journal of Glaciology*, *58*(207), 151–164. https://doi.org/10.3189/2012JoG11J163

753 Eberhard, L. A., Sirguey, P., Miller, A., Marty, M., Schindler, K., & Stoffel, A. (2021).
754 Intercomparison of photogrammetric platforms for spatially continuous snow depth

mapping. *The Cryosphere*, *15*, 69–94. https://doi.org/10.5194/tc-15-69-2021

Essery, R., Morin, S., Lejeune, Y., & Ménard, C. B. (2013). A comparison of 1701 snow models using observations from an alpine site. *Advances in Water Resources*, *55*, 131–148. https://doi.org/10.1016/j.advwatres.2012.07.013

Freudiger, D., Kohn, I., Seibert, J., Stahl, K., & Weiler, M. (2017). Snow redistribution for the hydrological modeling of alpine catchments. *Wiley Interdisciplinary Reviews: Water*, *4*(5), e1232. https://doi.org/10.1002/wat2.1232

Gascoin, S., Hagolle, O., Huc, M., Jarlan, L., Dejoux, J. F., Szczypta, C., Marti, R., & Sánchez, R. (2015). A snow cover climatology for the Pyrenees from MODIS snow products. *Hydrology and Earth System Sciences*, *19*(5), 2337–2351. https://doi.org/10.5194/hess-19-2337-2015

Gascoin, S., Grizonnet, M., Bouchet, M., Salgues, G. & Hagolle, O. (2019). Theia Snow collection: high-resolution operational snow cover maps from Sentinel-2 and Landsat-8 data, *Earth System Science Data*. *11*(2), 493–514. doi: 10.5194/essd-11-493-2019.

Girotto, M., Musselman, K. N., & Essery, R. L. H. (2020). Data Assimilation Improves Estimates of Climate-Sensitive Seasonal Snow. *Current Climate Change Reports*, 81–94. https://doi.org/10.1007/s40641-020-00159-7

Gleyzes, A., Perret L., Philippe Kubik, P. (2012). Pleiades system architecture and main performances. *Int. Archives of Photogrammetry, Remote Sensing and Spatial Information Sciences*, Vol. 39(1), pp. 537-542, Melbourne, Australia.

Hedrick, A., Marks, D., Havens, S., Robertson, M., Johnson, M., Sandusky, M., Marshall, H.-P., Kormos, P., Bormann, K., & Painter, T. (2018). Direct Insertion of NASA Airborne Snow Observatory-Derived Snow Depth Time Series Into the iSnobal Energy Balance Snow Model. *Water Resources Research*, *54*, 8045–8063. https://doi.org/10.1029/2018WR023190

Hersbach, H. (2000). Decomposition of the Continuous Ranked Probability Score for Ensemble Prediction Systems. *Weather and Forecasting*, *15*, 559–570. https://doi.org/10.1175/1520-0434(2000)015<0559:DOTCRP>2.0.CO;2

Kitagawa, G. (1996). Monte Carlo filter and smoother for non-Gaussian nonlinear state space models, *J. Comput. Graph. Stat.*, 5, 1–25.

Lafaysse, M., Cluzet, B., Dumont, M., Lejeune, Y., Vionnet, V., & Morin, S. (2017). A multiphysical ensemble system of numerical snow modelling. *Cryosphere*, *11*(3), 1173–1198. https://doi.org/10.5194/tc-11-1173-2017

Largeron, C., Dumont, M., Morin, S., Boone, A., Lafaysse, M., Metref, S., Cosme, E., Jonas, T., Winstral, A., Margulis, S. A., & Raleigh, M. (2020). Toward Snow Cover Estimation in Mountainous Areas Using Modern Data Assimilation Methods : A Review. *Frontiers in Earth Science*, *8*(September). https://doi.org/10.3389/feart.2020.00325

Luce, C., Staab, B., Kramer, Ma., Wenger, S., Isaak, D., & McConnell, C. (2014). variability in the Pacific Northwest. *Water Resources Research*, *50*, 1–16. https://doi.org/10.1002/2013WR014329.Received

Magnusson, J., Winstral, A., Stordal, A., Essery, R., & Jonas, T. (2017). Improving physically based snow simulations by assimilating snow depths using the particle filter. *Water Resources Research*, *53*, 1125–1143. https://doi.org/10.1002/2016WR019092.Received

Margulis, S. A., Fang, Y., Li, D., Lettenmaier, D. P., & Andreadis, K. (2019). The utility of infrequent snow depth images for deriving continuous space-time estimates of seasonal snow water equivalent. *Geophysical Research Letters*, *2015*, 2019GL082507. https://doi.org/10.1029/2019GL082507

Margulis, S. a., Girotto, M., Cortés, G., & Durand, M. (2015). A Particle Batch Smoother Approach to Snow Water Equivalent Estimation. *Journal of Hydrometeorology*, *16*(May 2015), 150504130725006. https://doi.org/10.1175/JHM-D-14-0177.1

Marti, R., Gascoin, S., Berthier, E., De Pinel, M., Houet, T., & Laffly, D. (2016). Mapping snow depth in open alpine terrain from stereo satellite imagery. *Cryosphere*, *10*(4), 1361–1380. https://doi.org/10.5194/tc-10-1361-2016

Menard, C. B., Essery, R., Krinner, G., Arduini, G., Bartlett, P., Boone, A., Brutel-Vuilmet, C., Burke, E., Cuntz, M., Dai, Y., Decharme, B., Dutra, E., Fang, X., Fierz, C., Gusev, Y., Hagemann, S., Haverd, V., Kim, H., Lafaysse, M., Marke, T., Nasonova, O., Nitta, T., Niwano, M., Pomeroy, J., Schädler, G., Semenov, V. A., Smirnova, T., Strasser, U., Swenson, S., Turkov, D., Wever, N. and Yuan, H. (2021). Scientific and Human Errors in a Snow Model Intercomparison, *Bulletin of the American Meteorological Society*, *102*(1), E61–E79. doi: 10.1175/bams-d-19-0329.1.

Quéno, L., Vionnet, V., Dombrowski-etchevers, I., Lafaysse, M., Dumont, M., Cnrs, F., Umr, C., & Martin, S. (2016). Snowpack modelling in the Pyrenees driven by kilometric- resolution meteorological forecasts. *The Cryosphere*, 1571–1589. https://doi.org/10.5194/tc-10-1571-2016

Raleigh, M. S., Lundquist, J. D., & Clark, M. P. (2015). Exploring the impact of forcing error characteristics on physically based snow simulations within a global sensitivity analysis framework. *Hydrology and Earth System Sciences*, *19*(7), 3153–3179. https://doi.org/10.5194/hess-19-3153-2015

Rasmussen, R., Baker, B., Kochendorfer, J., Meyers, T., Landolt, S., Fischer, A., Black, J., Thériault, J., Kucera, P., Gochis, D., Smith, C., Rodica, N., Hall, M., Ikeda, K., & Gutmann, E. (2012). How well are we measuring snow? *American Meteor*, *June*, 811–830. https://doi.org/10.1175/BAMS-D-11-00052.1

Revuelto, J., Jonas, T., & López-Moreno, J. I. (2016). Backward snow depth reconstruction at high spatial resolution based on time-lapse photography. *Hydrological Processes*, *30*(17), 2976–2990. https://doi.org/10.1002/hyp.10823

Revuelto, J., Lecourt, G., Lafaysse, M., Zin, I., Charrois, L., Vionnet, V., Dumont, M., Rabatel, A., Six, D., Condom, T., Morin, S., Viani, A., & Sirguey, P. (2018). Multi-Criteria Evaluation of Snowpack Simulations in Complex Alpine Terrain Using Satellite and In Situ Observations. *Remote Sensing*, *10*(8), 1171. https://doi.org/10.3390/rs10081171

Rodell, M., & Houser, P. (2004). Updating a Land Surface Model with MODIS-Derived Snow Cover. *Journal of Hydrometeorology*, *5*, 1064–1075. https://doi.org/10.1175/JHM-395.1

Salomonson, V. V, & Appel, I. (2004). Estimating fractional snow cover from MODIS using the normalized difference snow index. *Remote Sensing of Environment*, *89*, 351–360. https://doi.org/10.1016/j.rse.2003.10.016

Shaw, T., Caro, A., Mendoza, P., Ayala, Á., Gascoin, S., & Mcphee, J. (2020). The Utility of Optical Satellite Winter Snow Depths for Initializing a Glacio-Hydrological Model of a High-Elevation , Andean Catchment. *Water Resources Research*. https://doi.org/10.1029/2020WR027188

Smyth, E. J., Raleigh, M. S., & Small, E. E. (2019). Particle Filter Data Assimilation of Monthly Snow Depth Observations Improves Estimation of Snow Density and SWE Water Resources Research. *Water Resources Research*, *4*, 1296–1311. https://doi.org/10.1029/2018WR023400

Smyth, E. J., Raleigh, M. S., & Small, E. E. (2020). Improving SWE estimation with data assimilation: The influence of snow depth observation timing and uncertainty. *Water Resources Research*, 56. https://doi.org/10.1029/2019WR026853

Szczypta, C., Gascoin, S., Houet, T., Hagolle, O., Dejoux, J. F., Vigneau, C., & Fanise, P. (2015). Impact of climate and land cover changes on snow cover in a small Pyrenean catchment. *Journal of Hydrology*, *521*, 84–99. https://doi.org/10.1016/j.jhydrol.2014.11.060

Teufelsbauer, H. (2011). A two-dimensional snow creep model for alpine terrain. *Natural Hazards*, 481–497. https://doi.org/10.1007/s11069-010-9515-8

Thirel, G., Salamon, P., Burek, P., & Kalas, M. (2011). Assimilation of MODIS snow cover area data in a distributed hydrological model. *Hydrology and Earth System Sciences*, *8*, 1329–1364. https://doi.org/10.5194/hessd-8-1329-2011

Tuzet, F., Dumont, M., Lafaysse, M., Picard, G., Arnaud, L., Voisin, D., Lejeune, Y., Charrois, L., Nabat, P., & Morin, S. (2017). A multilayer physically based snowpack model simulating direct and indirect radiative impacts of light-absorbing impurities in snow. *The Cryosphere*, *11*, 2633–2653. https://doi.org/10.5194/tc-11-2633-2017

Vacquie, L. A., Houet, T., Sheeren, D., Munnik, N. De, Roussel, V., & Waddle, J. (2016). Adapting grazing practices to limit the reforestation of mountainous summer pastures : A process-based approach. *Environmental Modelling and Software*, *84*, 395–411. https://doi.org/10.1016/j.envsoft.2016.05.006

Vernay, M., Lafaysse, M., Hagenmuller , P., Nheili , R., Verfaillie , D., & Morin , S. (2019). The S2M meteorological and snow cover reanalysis in the French mountainous areas (1958 - present) [Data set]. AERIS. https://doi.org/10.25326/37#2019

Vernay, M., Lafaysse, M., Monteiro, D., Hagenmuller, P., Nheili, R., Samacoïts, R., Verfaillie, D., and Morin, S.: The S2M meteorological and snow cover reanalysis over the French mountainous areas, description and evaluation (1958–2020), Earth Syst. Sci. Data Discuss. [preprint], https://doi.org/10.5194/essd-2021-249, in review, 2021.

Viallon-galinier, L., Hagenmuller, P., & Lafaysse, M. (2020). Forcing and evaluating detailed snow cover models with stratigraphy observations. *Cold Regions Science and Technology*, *180*. https://doi.org/10.1016/j.coldregions.2020.103163

Vincent, L., Lejeune, Y., Lafaysse, M., Boone, A., Le Gac, E., Coulaud, C., Freche, G., Sicart, J.E. (2018). Interception of snowfall by the trees is the main challenge for snowpack simulations under forests. *In Proceedings of ISSW*, 705-710 http://arc.lib.montana.edu/snow-science/objects/ISSW2018_O08.4.pdf

Vögeli, C., Lehning, M., Wever, N., & Bavay, M. (2016). Scaling Precipitation Input to Spatially Distributed Hydrological Models by Measured Snow Distribution. *Frontiers in Earth Science*, *4*(December), 1–15. https://doi.org/10.3389/feart.2016.00108